Performance assessment of a coherent DIAL-Doppler fiber lidar at 1645 nm for remote sensing of methane and wind

Nicolas Cezard, Simon Le Mehaute, Julien Le Gouët, Matthieu Valla, Didier Goular, Didier Fleury, Christophe Planchat, Agnès Dolfi-Bouteyre

Research Article | Vol. 28, No. 15 / 20 July 2020 / Optics Express 22345
Optics EXPRESS

Performance assessment of a coherent DIAL-Doppler fiber lidar at 1645 nm for remote sensing of methane and wind

NICOLAS CEZARD,[1,2] SIMON LE MEHAUTE,[2] JULIEN LE GOUËT,[2] MATTHIEU VALLA,[2] DIDIER GOULAR,[2] DIDIER FLEURY,[2] CHRISTOPHE PLANCHAT,[2] AND AGNES DOLFI-BOUTEYRE[2]

[1] *ONERA/DOTA, Université de Toulouse, F-31055 Toulouse, France*
[2] *DOTA, ONERA, Université Paris Saclay, F-91123 Palaiseau, France*
[*] *nicolas.cezard@onera.fr*

Abstract: We report on the performances of a coherent DIAL/Doppler fiber lidar called VEGA, allowing for simultaneous measurements of methane and wind atmospheric profiles. It features a 10µJ, 200 ns, 20 kHz fiber pulsed laser emitter at 1645 nm, and it has been designed to monitor industrial methane leaks and fugitive emissions in the environment. The system performance has been assessed for range-resolved (RR) and integrated-path (IP) methane measurements in natural background conditions (i.e. ambient methane level). For RR measurements, the measured Allan deviation at τ=10 s is in the range of 3-20 ppm, depending of the aerosol load, at a distance of 150 m, with 30 m range resolution, and a beam focused around 150-200 m. For IP measurements, using a natural target at 2.2 km of distance, the Allan deviation at τ=10 s is in the range of 100-200 ppb. In both cases, deviation curves decrease as $\tau^{-1/2}$, up to 1000 seconds for the longest averaging time. Finally, the lidar ability to monitor an industrial methane leak is demonstrated during a field test.

1. Introduction

With a high warming global potential, methane is known as one of the most important greenhouse gas to monitor. It is also known, especially for oil & gas industrial activities, as a dangerous and explosive gas in the air, which can put people in danger during incidental circumstances. In the last decade, several massive methane leaks have occurred in the world (for instance in 2015 at Aliso Canyon, California), requiring preventive human evacuations, and implying serious difficulties in crisis control. In extreme cases, methane explosions (so-called blowouts) have also occurred, like in the *Deepwater Horizon* platform in 2010, leading to human casualties, and disastrous pollution of the ocean and the atmosphere. On the other side, fugitive methane emissions at low rates are also common in the industry. Although less dangerous for safety, they can represent large amounts over time and lead to significant environmental pollution. Therefore, they must be detected too, and limited as much as possible.

In order to develop new tools for methane leak monitoring, ONERA and Total have launched in 2013 a collaborative project called NAOMI (New Advanced Optical Methods Integration). A part of this project was dedicated to the development of an innovative lidar system, fibered, easy-to-deploy, and able to measure simultaneously range-resolved profiles of methane and wind speed. Knowledge of wind speed data is indeed essential for plume dispersion assessment. It may also lead, if used simultaneously with methane data, to autonomous leak rate estimation [1]. Between 2014 and 2019, this new lidar has been developed and tested. It has been called VEGA ("VEnt & GAz", french for "Wind & Gas").

#394553 https://doi.org/10.1364/OE.394553
Journal © 2020 Received 7 Apr 2020; revised 3 Jun 2020; accepted 18 Jun 2020; published 14 Jul 2020

Optics EXPRESS

Several CH_4 lidars, either range-resolved or path-integrated, have been reported before, employing direct detection systems and solid-state pulsed lasers like Optical Parametric Oscillators/Amplifiers (OPO/OPA) or Er:YAG cavities [2–8]. These systems generally show very good performances but exhibit a high number of free-space optics, for which alignment and long-term stability can be an issue, especially in harsh or vibrating environment conditions (e.g. outdoor conditions, vehicle-borne, airborne. . .). Other remote sensors have been developed using low-power semiconductor cw-modulated fiber systems (for instance [9–11]), but the provided measurements are not range-resolved along the laser line-of-sight. Moreover, none of the previous systems could measure wind speed simultaneously with methane concentration. As for gathering wind and gas functions in a single lidar, this has been reported before by several groups for the monitoring of CO_2 [12–14] and H_2O [15,16], either with solid-state or fiber architectures. However, to the best of our knowledge, this has never been done for methane, and furthermore, using a fiber lidar.

This paper first describes the lidar architecture in section 2, and details measurement principles for methane in range-resolved (RR) and integrated-path (IP) modes. Then in section 3, the lidar performances for methane measurements in IP and RR modes are evaluated in background conditions (i.e. ambient methane level). Finally, in section 4, an industrial field test is reported, and simultaneous profiles of methane concentration and radial wind speed (i.e. wind speed projected onto the laser line-of-sight), recorded during a controlled methane leak, are presented and discussed.

2. Lidar description and measurement principle

The lidar is pictured and schemed in Fig. 1. Its characteristics are summarized in Table 1.

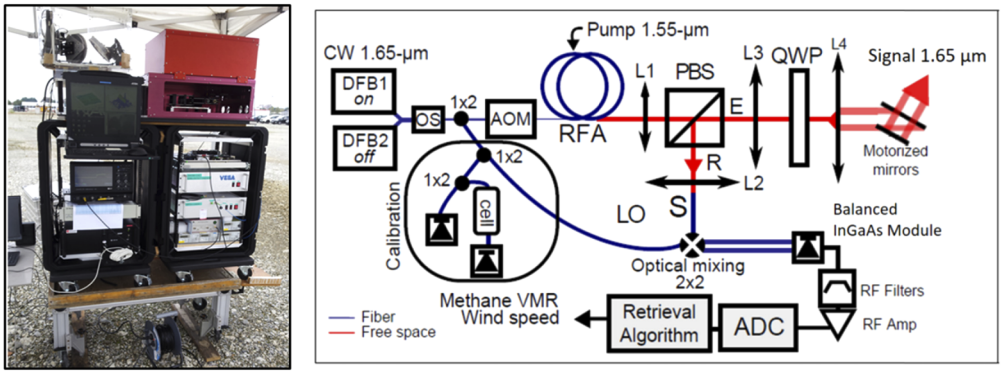

Fig. 1. Left: Picture of VEGA during the 2018 field test campaign (see section 4). Right: Lidar design, with following abbreviations. CW: Continuous Wave (emitter), DFB: Distributed FeedBack (diode), OS: 2×1 Optical Switch (2 inputs, 1 output), 1×2: fiber couplers (1 input, 2 outputs), AOM: Acousto-Optic Modulator, RFA: Raman Fiber Amplifier, L1-4: Lenses, PBS: Polarizing Beam-Splitter, QWP: Quarter-Wave Plate, E/R : Emission-Reception ports of the PBS, LO/S: Local Oscillator/Signal input ports of the 2×2x mixing coupler, RF: Radio Frequency (filters and amplifier), ADC: Analog to Digital Converter, Methane VMR: Methane Volume Mixing Ratio.

The laser source relies on a Master Oscillator Fiber Power Amplifier (MOFPA) architecture. The master lasers are two semi-conductor DFB (Distributed Feedback) diodes emitting about 15 mW of continuous wave (CW) radiation around 1645.54 nm. This wavelength corresponds to a well-known CH_4 absorption doublet line (merging at atmospheric pressure), represented in Fig. 2. The rationale for selecting this line, and the cross-section sensitivity to temperature

Optics EXPRESS

Table 1. Laser and Lidar parameters of the VEGA prototype

Laser		Lidar	
Energy	10 µJ	ON-OFF switch rate	5-10 Hz
Pulse duration	200 ns	Range resolution	30 m
Repetition rate	20 kHz	Beam radius @ L4	~ 38 mm
Linewidth	6 MHz	AOM shift	80 MHz
Polarization	Linear	Detector	Balanced InGaAs
Tunability	± 30 GHz	Sampling rate	250 MHz
Side-mode suppression ratio (laser DFB / LO)	50 dB	Spectral integration window	15 MHz

($\sim 2 \times 10^{-7}$ ppm^{-1}.m^{-1}.K^{-1} at T=296 K and P=1 atm) are detailed in [17]. This line is identical to the one chosen for MERLIN satellite project [18]. The two DFB respectively provide ON and OFF wavelength for DIAL operation (Differential Absorption Lidar) with a high level of spectral purity (the side-mode suppression ratio (SMSR) specification is 50 dB). They can be accurately frequency-tuned to their operating point through their driving current (fine tuning, about 740 MHz/mA with a driver resolution of 10µA, hence 7 MHz) and driving temperature (coarse tuning, about 14.3 GHz/K, with 2 mK driver resolution, hence 28 MHz). A 2×1 Optical Switch (OS) driven at 5-10 Hz alternately selects each DFB for optical amplification. Typically 2000 laser pulses are transmitted at the ON-line frequency before switching to the OFF-line, and so on. At the OS exit port, a part of the CW signal is taken off, while the remaining experiences an 80 MHz frequency-shift in an Acousto-Optic Modulator (AOM) and enters into a Raman Fiber Amplifier (RFA). The taken off part is divided in two, one part providing the Local Oscillator (LO) phase reference for heterodyne detection, and the other part being used for spectral calibration.

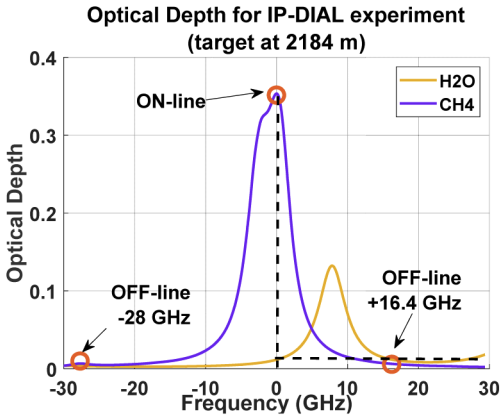

Fig. 2. Optical depth spectra of CH_4 and H_2O molecules for the IP-DIAL experiment discussed in section 3 (assuming 1% volume mixing ratio for H_2O). The spectra are represented on a frequency axis, centered on the absorption peak wavelength at 1645.543 nm (ON-line frequency throughout this paper). The OFF-line frequency was set either at -28 GHz (very small contribution of H_2O) or at +16.4 GHz (differential H_2O optical depth cancelled to zero by equalizing ON and OFF H_2O cross sections). The absorption cross sections have been calculated using HITRAN 2008 database [24].

A Raman Fiber Amplifier is used for amplification, because Erbium-doped fiber amplifiers, commonly used in coherent wind lidars around 1550 nm, do not have sufficient gain at 1645 nm. The Raman frequency shift in silica is about 13 THz, i.e. 100 nm near 1.55µm. Therefore, by choosing a 1545 nm pump wavelength for the amplifier, Stimulated Raman Scattering (SRS)

Optics EXPRESS

can provide gain to the 1645 nm seed signal [19,20]. As this paper focuses on the lidar system performances, the RFA internal architecture and physics shall not be detailed here, but it will be described in details in a separate paper (in preparation). Globally, the RFA acts as a pulsed amplifier with an overall gain of about 40 dB. The exit fiber is polarization maintaining and single-mode (PM-SM), allowing the output beam to propagate with an optimal spatial quality (M^2 ~1). Eventually, the fiber laser delivers linearly polarized 10 µJ, 200 ns pulses at a pulse repetition frequency (PRF) of 20 kHz. The pulse energy being currently limited by Brillouin effects in the amplifier fiber, a high repetition rate has been selected to increase the measurement quality using pulse averaging. The maximum lidar range (pulse overlapping limit) is c/(2PRF) =7.5 km, which is far enough for a 10 µJ system. The PRF setting may decrease in the future as the pulse energy increases. The pulse spectral width has been measured to be nearly Fourier-transform limited (6 MHz) and it is thus suitable for heterodyne detection.

The RFA output beam is collimated by a lens L1 and directed to a Polarizing Beam Splitter (PBS). Associated with a quarter wave-plate (QWP), the PBS allows separating the emission path (E) and reception path (R). After the PBS, the beam is expanded by the telescope lenses L3-L4, up to a beam radius of 38 mm. It is then sent to the atmosphere using a motorized two-mirror angular scanner system. The return signal (S) arises from Mie backscattering on atmospheric aerosols. It is collected through the same optics as for emission (monostatic configuration), and since the polarization is rotated by 90° after crossing two times the QWP, it is directed by the PBS to lens L2, which focuses the signal into a SM fiber. The signal is then mixed with the LO using a 50:50 coupler, and the two coupler's outputs are finally fed to a balanced AC-coupled InGaAs detection module (150 MHz bandwidth). The interference between the signal and the LO generates the heterodyne signal, i.e. a radio-frequency (RF) beat note oscillating at frequency $f_{AOM}+f_{DOP}$, f_{AOM} and f_{DOP} being respectively the AOM frequency shift and the Doppler frequency shift (positive or negative) induced by the wind. The RF signal is eventually passband-filtered (10-100 MHz), amplified, and digitized through an Analog-to-Digital Converter (ADC) at 250 Ms/s.

The recorded data are then processed as detailed in [21]. For each lidar pulse, the Power Spectrum Density (PSD) of the lidar signal is computed. The PSDs are then averaged over 2000 pulses, i.e. during 100 ms at 20 kHz repetition rate. Then, the zero-order and first-order moments of the averaged PSD are calculated over a narrow band (B=15 MHz here) located around the detected PSD frequency peak. The zero-order moment, after subtraction of the noise component, is used to compute the signal Carrier-to-Noise Ratio (CNR), while the first order moment gives the PSD centroid frequency, proportional to the Doppler shift, hence to the so-called radial wind speed (i.e. wind speed projected onto the lidar line-of-sight). Integrating the PSD over a very narrow band B to compute the CNR allows filtering out any possible laser spectral impurities outside of the band, which alleviates the power beam spectral purity issue compared to direct detection lidars (15 MHz is far below the spectral-filtering capacity of optical filters). High LO purity is still needed however, to ensure that the optical lidar spectrum translates into the RF domain with high fidelity (i.e. without spectral leaking effects), but this condition is well verified here (the LO purity is specified to 50 dB).

The CNR indicator is commonly used in coherent lidar systems. For an atmospheric target at distance z, it can be expressed as [22]:

$$CNR = \eta \frac{E}{h\nu B} \frac{c\beta}{2} \frac{A}{z^2} T_{atm}^2 \tag{1}$$

where η represents the overall lidar efficiency factor, E the laser pulse energy, h the Planck's constant, ν the laser frequency, B the PSD integration bandwidth, c the speed of light, β the aerosols backscattering coefficient, A the receiver aperture area, and T^2_{atm} the total atmospheric transmission (back and forth). The CNR can thus be used to compute the range-resolved (RR) profile of methane Volume Mixing Ratio (VMR). Assuming same conditions, at ν_{ON} and ν_{OFF}, for the absorption coefficient of any other gas than methane, the range-resolved methane VMR

Optics EXPRESS

simply writes as:

$$\bar{C}_{RR}(z) = \frac{1}{2\Delta z \Delta\sigma} \ln\left(K_\beta \frac{CNR(z,\lambda_{OFF})}{CNR(z,\lambda_{ON})} \frac{CNR(z+\Delta z,\lambda_{ON})}{CNR(z+\Delta z,\lambda_{OFF})}\right) \quad (2)$$

This is the classical DIAL equation [23] where the CNR is used to describe the return signal power. In this expression, $\bar{C}$stands for the average methane VMR, in ppm, within the range gate [z-Δz/2, z+Δz/2], Δz is the lidar range resolution ($\Delta z = cT_P/2 = 30$ m here), and Δσ is the methane differential absorption cross section between ON-line and OFF-line frequencies, computed here in $ppm^{-1}.m^{-1}$ units. We also introduce the perturbation factor K_β=[β(z,λ_{ON})β(z+Δz,λ_{OFF})]/[β(z,λ_{OFF})β(z+Δz, λ_{ON})]. This term accounts for possible spatial inhomogeneities of the backscattering coefficient. Because β varies smoothly with wavelength, K_β would be unity if λ_{ON} and λ_{OFF} measurements were made simultaneously. In practice, the small delay between both measurements can induce, in some situations (see section 3), slight time variations of K_β around unity, hence be responsible of an excess noise factor (generally unbiased) in RR-DIAL measurements.

In case that a hard-target is present on the line-of-sight at distance L, the hard target CNR is given by a similar equation as Eq. (1), where β is replaced by a factor proportional to the target albedo, noted ε here. From Eq. (1), it is then possible to estimate the Integrated-Path (IP) VMR of methane using the following IP-DIAL equation:

$$\bar{C}_{IP} = \frac{1}{2L\Delta\sigma} \ln\left(K_\varepsilon \frac{CNR(L,\lambda_{OFF})}{CNR(L,\lambda_{ON})} \frac{E_{ON}}{E_{OFF}} \frac{\nu_{OFF}}{\nu_{ON}} \frac{\eta_{ON}}{\eta_{OFF}}\right) \quad (3)$$

In this expression, the distance L can be easily estimated from the lidar data, since the hard target generally produces a high CNR peak at the target distance. E_{ON} and E_{OFF} are the emitted pulse energies at ON and OFF frequencies. They are monitored by digitizing and time-integrating the leakage signal generated by the small reflection of outgoing pulses on the PBS (a fiber is connected to the "free" PBS port of Fig. 1, unrepresented for clarity). The factor ν_{OFF}/ν_{ON} is very close from unity and could be omitted here, since ν_{ON} and ν_{OFF} differ at most by 30 GHz ($\delta\nu/\nu = 1.6\times10^{-4}$). The factor η_{ON}/η_{OFF} would also be unnoticeably close from unity if the heterodyne detection was perfectly shot-noise limited (ideal case). In our case, the detection is not strictly ideal, such that this term can be responsible of a small bias on the IP methane measurement (discussed in section 3). Finally the perturbation factor $K_\varepsilon=\varepsilon_{ON}/\varepsilon_{OFF}$ is similar as K_β in RR-DIAL measurement. It accounts for the possible small variation of the hard target's albedo, between ON and OFF measurements. Since target albedos are generally smooth functions of frequency, the mean value of K_ε is expected to be unity (it induces no measurement bias), but small timescale albedo variations could be responsible of an excess noise factor in IP-DIAL measurements.

3. Performance assessment

In this section, we report on the lidar performances measured in background environmental conditions (ambient methane level). The performance for IP-DIAL and RR-DIAL measurements are discussed as a function of the averaging time, using Allan deviation curves. In the RR-DIAL case, performances as a function of lidar range are also presented. Simple models are proposed to compute expected random errors for these measurements, and the results are compared to the observed (statistical) random errors. In this part, we introduce the Relative Random Error (RRE) of a measured random variable X as $RRE(X) = \sigma_X/\langle X\rangle$, where $\langle X\rangle$ and σ_X are the mean and standard deviation of X. We also define the covariance degree between variables X and Y by $\rho_{XY}=\mathrm{cov}(X,Y)/(\sigma_X\sigma_Y)$.

Optics EXPRESS

3.1. Integrated path methane measurements

To perform IP-DIAL measurements, the lidar has been placed on the building rooftop at ONERA's laboratory in Palaiseau (20 km south of Paris), aiming at hard targets (trees) located at 2.2 km of distance (L=2184 m below). IP-DIAL estimates have been computed using a simplified version of Eq. (3) (with K_ε=1, ν_{ON}/ν_{OFF}=1, η_{ON}/η_{OFF}=1), and an averaging time of 0.2 seconds for each IP estimate (time required for 2000 pulses ON and 2000 pulses OFF). The ON-line frequency was set at the top of the absorption line and the OFF-line frequency at +16.4 GHz from the top (see Fig. 2) so as to cancel water-vapor interference. The methane cross-section was also temperature-corrected, using the temperature sensitivity coefficient given in section 1. The Fig. 3 shows the Allan deviation of two datasets recorded on 29/09/2019 with a high CNR (+5 dB) and on 14/11/2019 with a lower CNR (-0.1 dB). The Allan deviation slopes in log scale are very close from -1/2, up to 1000 seconds for the longest record, indicating that the measurement noise behaves like a white noise, and that there is no measurable drift up to these timescales. At high CNR (green curve), the measurement precision is below 100 ppb after 10 s averaging, with extrapolated values of 30 ppb for 100 seconds, or 10 ppb for 1000 seconds (17 min).

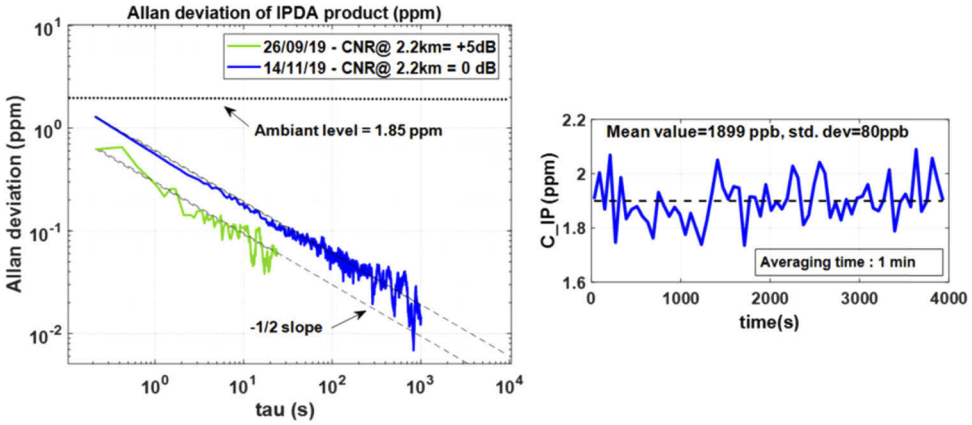

Fig. 3. (Left): Allan deviation of the IP-DIAL measurement recorded on 26/09/2019 (green) and 14/11/2019 (blue). The -1/2 slope coefficients show that the measurements are stationary at least up to their maximum averaging times (1000 s for the blue curve). The horizontal dashed line indicates the approximate ambient level. (Right): Time series of the IP-DIAL measurement recorded on 14/11/2019, with a 1-min averaging window.

The Fig. 3 (right) also shows the IP-DIAL time record at low CNR (blue curve), for 1 min time-averaging. This measurement yields a CH_4 volume mixing ratio of 1900 +/-80 ppb (4% relative random error), which is consistent with the expectation (typically between 1800 and 2200 ppb). A small bias subsists on this measurement, because the factor η_{ON}/η_{OFF} is not strictly equal to one in our case. Indeed, the coherent detection is not exactly shot-noise limited (we have measured that 90% of the total noise power come from the shot noise, and 10% from the detector intrinsic noise), and there is a small unbalance (by maximum 5%) between ON and OFF local oscillator powers. The combination of these imperfections lead to an expected bias in the magnitude of 5.10^{-3} in optical depth (η_{ON}/η_{OFF}=1.005), hence 20 ppb for the presented IP-DIAL measurement. Though this bias remains small, it will be undoubtedly useful in the future to perform a detailed accuracy assessment of the lidar, by comparing IP-DIAL measurements with a calibrated reference instrument. The current result is however consistent enough for checking the lidar accuracy, in the perspective of industrial plume monitoring with expected methane VMR high above the ambient level.

Optics EXPRESS

In a simple IP-DIAL error model, we can consider that errors on energy measurements E_{ON} and E_{OFF} are negligible (indeed the observed RREs on these variables are in the magnitude of 1% or less). The terms ν_{OFF}/ν_{ON} and η_{ON}/η_{OFF} are instrumental constants, with no statistic nature, and do not enter into the random error budget. Using a Taylor expansion of the variance of $\ln(CNR_{OFF}/CNR_{ON})$, the IP-DIAL random error, when averaging N_{avg} successive values, can then be written as :

$$\sigma_{IP} = \frac{\sqrt{RRE^2_{K_\varepsilon} + RRE^2_{CNR_{ON}} + RRE^2_{CNR_{OFF}} - 2\rho_{CNR_{ON}CNR_{OFF}}(RRE_{CNR_{ON}}RRE_{CNR_{OFF}})}}{2L\Delta\sigma\sqrt{N_{avg}}} \quad (4)$$

Here the variables CNR_{ON} and CNR_{OFF} are the hard-target CNR at distance L. Generally, they are correlated random variables. Indeed, since the ON and OFF optical frequencies are very close, the hard-target-induced speckle pattern experienced by the two frequencies, can be partially time-correlated. The correlation time depends on system parameters, like the switching delay between ON and OFF measurements (0.1 second here), but also on hard-target parameters like its motion at the wavelength scale (leaves motion on trees for instance). The correlation degree is difficult to predict, but it can be measured statistically from a large number of CNR observations. The variability of K_ε reflects albedo variations during the time delay between ON and OFF measurements. Unless the target is moving or shaking, such variations should be very small, and the random error associated with K_ε be negligible. The Table 2 indicates the mean values, RREs and correlation degrees of CNR_{ON} and CNR_{OFF} for the two datasets shown on Fig. 3. Very significant correlation degrees are observed (30% and 57%) between CNR_{ON} and CNR_{OFF}. The reason for observing differences in correlation degrees could be an effect of structural and motion differences between each experiment's scattering target (for instance, differences are expected between shaking leaves on trees and a motionless surface). Nevertheless, once taken into account, the IP-DIAL standard deviations, observed from data and computed from the above formula (with $RRE_{K\varepsilon}$=0), are seen to be very close. In the first row (14/11/2019 experiment), the observed excess error (0.2ppm) could be an effect of the random error of Kε. Indeed, a smaller correlation degree suggests a more dynamic hard target, which is consistent with higher albedo variations in a given delay.

Table 2. Hard target error analysis, for the minimal averaging time of 0.2 s (N_{avg}=1).

	Observed CNR ON		Observed CNR OFF		Observed ρ_{cov}	IP-DIAL Standard deviation	
	Mean	RRE	Mean	RRE		$\sigma_{observed}$	$\sigma_{computed}$
14/11/2019	0.77	28%	1.2	28%	30%	1.5 ppm	1.3 ppm
26/09/2019	2.9	14%	4.2	15%	57%	0.6 ppm	0.6 ppm

3.2. Range-resolved methane measurements

In order to assess the lidar performance in RR-DIAL mode, we now consider CNR observations from atmospheric range-gates (aerosols backscattering), instead of the hard-target range-gate. The range-resolved methane VMRs are computed from Eq. (2) with K_β=1. The Fig. 4 shows the Allan deviation of RR-DIAL methane measurements on a 30 m range-gate centered at 150m of distance. Three data sets are presented. Two of them correspond to the same experiments presented in Fig. 3, and in both cases the atmospheric aerosol load (hence the CNR) was low. However, the beam was focused at 180 m for the blue curve and at 400m for the green curve (hence the CNR at 150 m is lower for the green curve). The third deviation curve, in red, was recorded with a high aerosol load (in an industrial test site, as detailed in section 4), and a beam focused at 150 m. These three curves first show that the measurement precisions for range-resolved measurements are, quite logically, much lower than for integrated-path measurement. For instance, for two

Optics EXPRESS

similarly focused beams, the precision at high CNR (red curve) can reach the ambient level (2 ppm) for an integration time of about 40 sec, whereas it would take 13 min at low CNR (blue curve). At the scale of 1s, the precision is measured in the range of 10 to 50 ppm for beams focused at 150-200 m. We will see in the next section that this proves to be enough to detect and quantify small leaks in an industrial site. The Allan deviation slope coefficients, in log scale, are close to -1/2, with no measurable drift up to 1000 seconds for the longest time record. This suggests that sub-ambient precision should be possible with VEGA using longer averaging times. Also, the results shown here are for a 30 m range resolution. Therefore, the precision could also be improved using larger space-averaging.

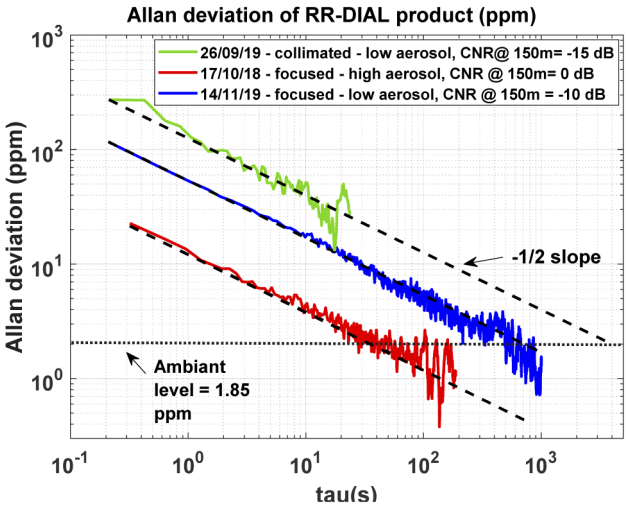

Fig. 4. Allan deviation of RR-DIAL measurements recorded on 26/09/2019 (green), 14/11/2019 (blue), and 17/10/2018. The horizontal dashed line indicates the approximate ambient level.

Again, a simple error model can be derived. In natural background conditions (ambient methane level), the assumption can be made that the variations of mean CNRs from a range-gate to the next one are small (CNR(z) ≈ CNR(z+Δz)). The RR-DIAL random error can then be approximated by:

$$\sigma_{RR}(z) = \frac{1}{2\Delta z \Delta\sigma}\frac{1}{\sqrt{N_{avg}}}\sqrt{2}\sqrt{RRE^2_{K_\beta}/2 + RRE^2_{CNR_{ON}(z)} + RRE^2_{CNR_{OFF}(z)}} \quad (5)$$

This expression is very similar to the IP-DIAL error formula. However, the range gate distance Δz replaces the hard-target distance L, and a factor $2^{1/2}$ accounts for the above assumption that CNR(z)≈CNR(z+Δz) for both ON and OFF frequencies. The random error on K_β accounts for possible residual variability of the double ratio K_β, as explained in section 2. Last, there is no more correlation between CNR_{ON} and CNR_{OFF} random variables. Indeed, since the aerosol spatial distribution changes very quickly (typically a few ns) at the wavelength scale, each laser pulse at 20 kHz experiences a completely decorrelated speckle pattern. Under such conditions, the random error for each CNR measurement is given by Gibert et al. [13]:

$$RRE_{CNR} = \frac{1}{\sqrt{N_{pulses}}}\frac{1}{\sqrt{M_T}}\left(1 + \frac{1}{\langle CNR\rangle}\right) \quad (6)$$

Where N_{pulses} is the number of laser pulses used for each CNR estimate (here N_{pulses}=2000), while M_T is the number of independent realizations of speckle patterns associated to the pulse

Optics EXPRESS

waveform. In the case (verified here) where the range-gate duration is taken equal to the pulse duration, M_T is in the magnitude of the ratio between the pulse duration T_P and the coherence time τ_{coh} of the pulse waveform: $M_T \approx T_P/\tau_{coh}$. The coherence time can be evaluated by $\tau_{coh} \approx 1/(2\pi f_2)$ where f_2 is the frequency FWHM (at $1/e^2$ from the maximum) of the emitted pulse. The number M_T is then approached by $M_T \approx 2\pi f_2 T_P$. With T_P=200 ns and a spectral width measured at f_2=2.5 MHz, we obtain $M_T \approx 3$ speckle patterns.

The expected random error for range-resolved methane measurements can thus be computed and compared with the observed random errors. The result is shown on Fig. 5 where the errors (calculated with $RRE_{K\beta}$=0) are plotted as a function of distance, for an averaging time of 20 seconds. The green and blue curves are computed from the same datasets already presented in Fig. 4. For the beam focused at farthest range (400m, green curve), there is a very good agreement between observed and predicted errors. For the beam focused at close range (180 m in blue), the agreement is reasonable (within 40%) below 350m, but above 400m the observed error reaches a floor. This is due to the fact that the mean CNR becomes very low (below -20 dB), and consequently the estimation procedure produces a large number of outliers. This issue could be solved in future works by filtering the outliers and/or by averaging a larger number of individual pulses for each CNR estimate, though the time resolution would decrease accordingly. The red curve is computed from a dataset recorded with a beam focused at 150 m and a high aerosol load. Only the first hundred meters are plotted for clarity. The observed error around the focus point is higher than the theoretical expectation by approximately a factor of 2-2.5. This excess error is attributable to $RRE_{K\beta}$. Indeed, this measurement has been made on an industrial test site (see section 4) with irregular dusty conditions around the focus point (dust emission from a stack). As previously noted by M. Hardesty [15], in such dynamic conditions, the assumption that the aerosol backscattering coefficient cancels in the RR-DIAL estimate may be violated, because of the small delay between ON and OFF measurements. The associated error K_β would tend to be unbiased, but nevertheless it is expected to induce an excess noise factor, as observed here. This issue could be solved by increasing the ON-OFF switching rate. The switching rate was limited to 10 Hz at the time of these measurements because of data collection timing issues, but the problem is currently solved, and a faster switching rate (typically 500 Hz) will be possible in future work.

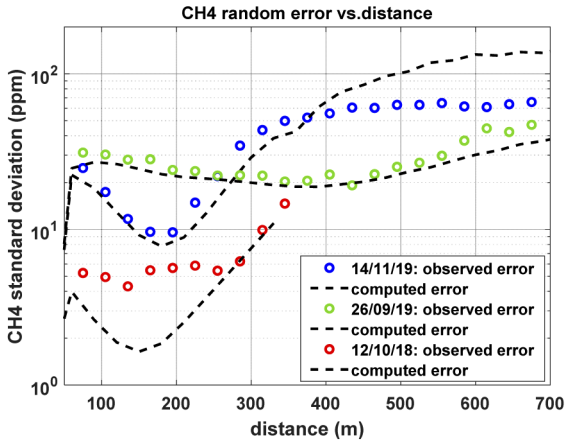

Fig. 5. Observed and expected standard deviations, as a function of range, for range-resolved methane measurements obtained with various aerosols and focusing conditions.

Optics EXPRESS

4. Detection of industrial methane leaks

During two field campaigns, conducted in October 2018 and October 2019, VEGA has been tested against controlled methane leaks in an industrial test site named TADI (Total Anomaly Detection Initiative), located in Lacq, southwest of France. TADI is a unique facility allowing controlled releases of methane from several leak points (tanks, stack. . .) with various leak rates between 0.3 g.s^{-1} and 300 g.s^{-1} [25]. During these two campaigns, numerous leaks have been generated, and more than 50 have been monitored by VEGA under a variety of measurement protocols (single or scanning line of sight, single or scanning On-line wavelength) and conditions (low/high leak rates, various aerosol loads, wind, temperature, and humidity conditions). A thorough summary of all the campaign results is therefore beyond the scope of this paper. We shall rather detail here a single experiment demonstrating the lidar capacity to characterize an industrial leak rate with simultaneous range-resolved profiles of methane volume mixing ratio and radial wind speed.

The presented experiment, recorded on 10/10/2018 for a medium-range leak rate (10 g/s), is chosen here because a sonic anemometer was located in the vicinity of the leak point, making the comparison with the wind profiles measured with VEGA more reliable. The leak point was the top of a 6m-high stack, located at a distance of 200m from the lidar. The lidar was operating in outdoor conditions (see Fig. 1-left), and aimed about 50 cm above the stack, with a sky background. Consequently only the RR-DIAL mode was possible for this test (no available echo for IP-DIAL measurement). The ON-line and OFF-line frequencies are shown on Fig. 2 (OFF-line at -28 GHz here). The laser beam was focused at 200 m from the lidar site, in order to enhance methane sensitivity above the stack. The Fig. 6 shows the methane VMR and radial wind speed profiles, measured simultaneously, as a function of distance and time, with averaging times of 10s and 1s respectively. The wind is computed by processing only the reference OFF-line signal. Because the beam was focused, and the CNR was quite low for this test, the noise increases quickly with distance, such that the lidar range is in the magnitude of 300-400 m here. Both figures are over-sampled in distance by a factor of five for better visibility (6m sample rate, while the lidar range resolution is Δz=30 m). Numeric mixing ratio values must be interpreted as mean values over the range resolution. In this case, because the plume diameter (typically D $\approx$ 0.5-1 m) above the stack was much smaller than the lidar range resolution, the real plume concentration is expected to be higher that the measured one by a factor of about $\Delta z/D$ ($C_{real} \approx C_{measured} * \Delta z/D$). In practice, it is possible to scan the laser line-of-sight across the plume to measure the diameter D, and calculate the correction factor $\Delta z/D$. Here, for more clarity and data fidelity, we report values of measured concentrations ($C_{measured}$).

The Fig. 7 (left plot) shows two methane range profiles, at VMR peak and before the gas release (corresponding to the white vertical dashed lines in Fig. 6). Behind the plume (blue curve), the noise rises very quickly and produces spurious peaks because the plume absorbs most of the ON-line laser light. At the VMR peak, the detection contrast is seen to be comfortable. Comparing the peak value at 200m (730 ppm) to the standard deviation before gas release (σ=24 ppm around 200 m) suggests a detection signal to noise ratio in the magnitude of 30 for this 10g/s test. This in turn suggests that in the same measurement conditions, a leak rate limit of 0.3 g/s would have been detected (actually, under more favorable CNR conditions, VEGA did perform successful plume measurements from 0.3 g/s leaks with only 1 second averaging time). The right plot shows the radial wind speed time series, recorded with the lidar (blue curve) at a distance of 200m, just above the stack. It corresponds to the black horizontal dashed line in Fig. 6. It is compared with the measurement performed by the sonic anemometer (Metek Sonic 3D, sample period 1 min), located at 10 m-height on a meteorological mast located about 30 m away from the stack. Since the sonic anemometer provides the horizontal wind vector, its measurements (black circles) have been projected onto the lidar line of sight to allow for comparison with the lidar data. The agreement between both measurements is fairly good (residual rms = 0.44 m/s) and

Optics EXPRESS

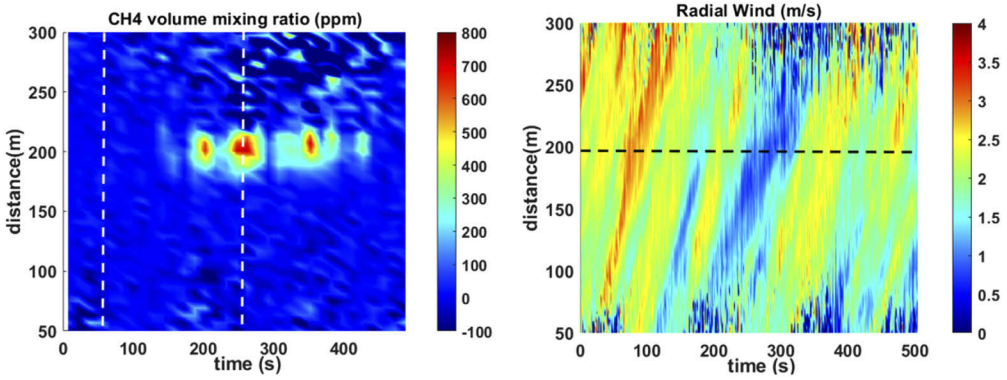

Fig. 6. CH_4 volume mixing ratio profile (10 s averaging) and radial wind speed profile (1 s averaging), measured simultaneously with VEGA during a 10 g/s leak rate detection test on 10/10/2018 at Total's TADI test site of Lacq (France). The first 50 m (not shown) correspond to the lidar blind zone (strong scattering signal from the lidar optics).

gives confidence in the wind measurements performed with VEGA. Some point discrepancies can be seen however, probably due to the wind field inhomogeneity in space and time, as shown by the measured wind map of Fig. 6.

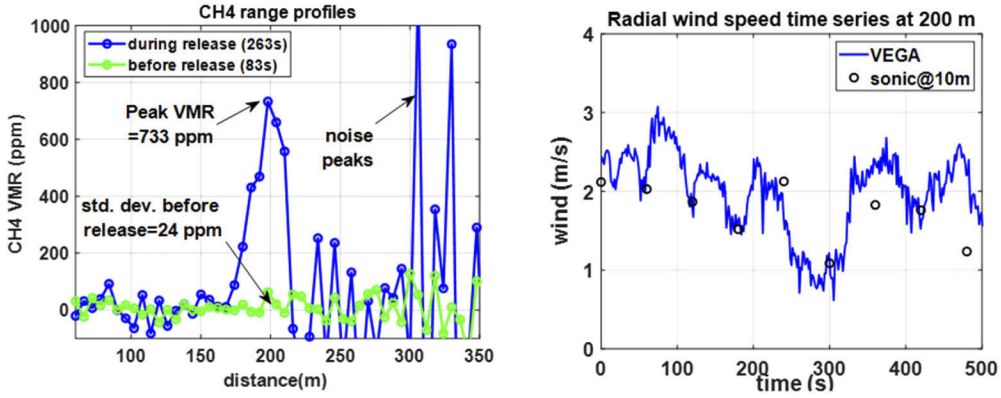

Fig. 7. Left: CH_4 volume mixing ratio range profiles measured at the VMR peak (263 s) and before the gas release (83 s). Right: Radial wind speed time series recorded just above the leak point by VEGA (at 200 m range), compared with a sonic anemometer located a few tens of meter away.

5. Conclusion

We have demonstrated simultaneous measurements of range-resolved profiles of methane concentration and radial wind speed with the fiber lidar VEGA. Wind measurements have shown a good agreement with a reference instrument, while methane IP measurements have been consistent with the expected value. This suggests that the lidar has a good accuracy for both wind and methane functions. The measurement precision for methane has been assessed in details, and random error models have shown to be in good agreement with statistically observed errors. In RR mode, the precision is in the magnitude of 3-20 ppm at 150m of distance (with focused beam), for averaging times below 10 seconds with 30 m range resolution. Allan deviation curves suggest that precisions below 2 ppm should be possible using averaging time between one and several

Optics EXPRESS

tens of minutes depending of aerosols and beam focus conditions. In IP mode at 2 km-range, our results suggest that a precision below 20 ppb (1%) could be obtained within typically 20 minutes averaging time. Finally, we have demonstrated that VEGA was suitable for detection and characterization of a methane leak on an industrial field in outdoor operation. This opens perspectives for future industrial leaks and fugitive emissions monitoring with this new fiber lidar tool. Another perspective is to make a synergetic use of simultaneously measured methane and wind data, in order to derive the leak rate in an autonomous way.

Funding

NAOMI (ONERA-Total).

Acknowledgments

The development of VEGA has been funded under NAOMI contract (ONERA-Total). Authors are thankful to numerous people involved in the development of VEGA Lidar, especially P. Benoit and G. Canat for the fiber laser source. Authors are also grateful to H. Delbarre for fruitful discussions, P.-Y. Foucher and X. Watremez for leading the NAOMI contract, O. Duclaux, C. Juery, X. Marcarian, and all the people of Total's TADI platform in Lacq for having made possible the field tests of VEGA.

Disclosures

The authors declare no conflicts of interest.

References

1. P. Weibring, M. Andersson, H. Edner, and S. Svanberg, "Remote monitoring of industrial emissions by combination of lidar and plume velocity measurements," Appl. Phys. B **66**(3), 383–388 (1998).
2. F. Innocenti, R. Robinson, T. Gardiner, A. Finlayson, and A. Connor, "Differential Absorption Lidar (DIAL) Measurements of Landfill Methane Emissions," *Remote Sens.* **9**(9), 953 (2017).
3. A. Amediek, G. Ehret, A. Fix, M. Wirth, C. Büdenbender, M. Quatrevalet, C. Kiemle, and C. Gerbig, "CHARM-F—a new airborne integrated-path differential-absorption lidar for carbon dioxide and methane observations: measurement performance and quantification of strong point source emissions," Appl. Opt. **56**(18), 5182–5197 (2017).
4. H. Riris, K. Numata, S. Li, S. Wu, A. Ramanathan, M. Dawsey, J. Mao, R. Kawa, and J. B. Abshire, "Airborne measurements of atmospheric methane column abundance using a pulsed integrated-path differential absorption lidar," Appl. Opt. **51**(34), 8296–8305 (2012).
5. T. F. Refaat, S. Ismail, A. R. Nehrir, J. W. Hair, J. H. Crawford, I. Leifer, and T. Shuman, "Performance evaluation of a 1.6-μm methane DIAL system from ground, aircraft and UAV platforms," Opt. Express **21**(25), 30415–30432 (2013).
6. K. Numata, S. Wu, and H. Riris, "Fast-switching methane lidar transmitter based on a seeded optical parametric oscillator," Appl. Phys. B **116**(4), 959–966 (2014).
7. J. Barrientos Barria, A. Dobroc, H. Coudert-Alteirac, M. Raybaut, N. Cézard, J.-B. Dherbecourt, T. Schmid, B. Faure, G. Souhaité, J. Pelon, J.-M. Melkonian, A. Godard, and M. Lefebvre, "Simultaneous remote monitoring of atmospheric methane and water vapor using an integrated path DIAL instrument based on a widely tunable optical parametric source," Appl. Phys. B: Lasers Opt. **117**(1), 509–518 (2014).
8. P. M. Burns, M. Chen, D. Pachowicz, S. Litvinovitch, F. Fitzpatrick, and N. W. Sawruk, "Single Frequency Er:YAG methane/water vapor DIAL source," in *Imaging and Applied Optics 2018 (3D, AO, AIO, COSI, DH, IS, LACSEA, LS&C, MATH, pcAOP)*, OSA Technical Digest (Optical Society of America, 2018), paper SW3H.2.
9. G. A. Wagner and D. F. Plusquellic, "Ground-based, integrated path differential absorption LIDAR measurement of CO_2, CH_4, and H_2O near 1.6 μm," Appl. Opt. **55**(23), 6292–6310 (2016).
10. T. Iseki, T. Hideo, and K. Kiyoshi, "A portable remote methane sensor using a tunable diode laser," Meas. Sci. Technol. **11**(6), 594–602 (2000).
11. J. T. Dobler, T. G. Pernini, N. Blume, T. S. Zaccheo, and M. Braun, "GreenLITE: a new laser-based tool for near-real-time monitoring and mapping of CO2 and CH4 concentrations on scales from 0.04-25 km2," Proc. SPIE **10406**, 1040604 (2017).
12. G. J. Koch, B. W. Barnes, M. Petros, J. Y. Beyon, F. Amzajerdian, J. Yu, R. E. Davis, S. Ismail, S. Vay, M. J. Kavaya, and U. N. Singh, "Coherent differential absorption lidar measurements of CO_2," Appl. Opt. **43**(26), 5092–5099 (2004).
13. F. Gibert, P. Flamant, D. Bruneau, and C. Loth, "Two-micrometer heterodyne differential absorption lidar measurements of the atmospheric CO2 mixing ratio in the boundary layer," Appl. Opt. **45**(18), 4448–4458 (2006).

Optics EXPRESS

14. S. Ishii, K. Mizutani, H. Fukuoka, T. Ishikawa, B. Philippe, H. Iwai, T. Aoki, T. Itabe, A. Sato, and K. Asai, "Coherent 2 μm differential absorption and wind lidar with conductively cooled laser and two-axis scanning device," Appl. Opt. **49**(10), 1809–1817 (2010).
15. R. M. Hardesty, "Coherent DIAL measurement of range-resolved water vapor concentration," Appl. Opt. **23**(15), 2545–2553 (1984).
16. M. Imaki, K. Hirosawa, T. Yanagisawa, S. Kameyama, and H. Kuze, "Wavelength selection and measurement error theoretical analysis on ground-based coherent differential absorption lidar using 1.53 μm wavelength for simultaneous vertical profiling of water vapor density and wind speed," Appl. Opt. **59**(8), 2238–2247 (2020).
17. N. Cézard, P. Benoit, and G. Canat, "1.6 micron fiber laser source for CH4 gas leak detection," EPJ Web Conf. **119**, 05010 (2016).
18. G. Ehret, P. Bousquet, C. Pierangelo, M. Alpers, B. Millet, J. B. Abshire, H. Bovensmann, J. P. Burrows, F. Chevallier, P. Ciais, C. Crevoisier, A. Fix, P. Flamant, C. Frankenberg, F. Gibert, B. Heim, M. Heimann, S. Houweling, H. W. Hubberten, P. Jöckel, K. Law, A. Löw, J. Marshall, A. Agusti-Panareda, S. Payan, C. Prigent, P. Rairoux, T. Sachs, M. Scholze, and M. Wirth, "MERLIN: A French-German Space Lidar Mission Dedicated to Atmospheric Methane," Remote Sens. **9**(10), 1052 (2017).
19. D. Mitchell, "Remote methane sensor using Tunable Diode Laser Spectroscopy (TDLS) via a 1W Raman Source," Proc. SPIE **7503**, 750350 (2009).
20. P. Benoit, N. Cézard, A. Durécu, A. Mussot, A. Kudlinski, and G. Canat, "Single-frequency Raman fiber amplifier emitting 11 μj 150 W peak-power at 1645 nm for remote methane sensing applications"," Proc. SPIE **9728**, 97281E (2016).
21. S. Le Méhauté, P. Benoit, N. Cézard, D. Goular, C. Planchat, M. Valla, A. Dolfi-Bouteyre, X. Watremez, and H. Delbarre, "All-fibered coherent-differential absorption lidar at 1.645 μm for simultaneous methane and wind-speed measurements," Proc. SPIE **10791**, 1079103 (2018).
22. T. Fujii and T. Fukuchi, *Laser Remote Sensing* (Taylor & Francis Group, 2005) pp 912
23. R. M. Measures, *Laser Remote Sensing, Fundamentals and Applications* (Wiley and Sons, 1984)
24. L. Rothman, I. Gordon, A. Barbe, D. Benner, P. Bernath, M. Birk, V. Boudon, L. Brown, A. Campargue, J. Champion, K. Chance, L. Coudert, V. Dana, V. Devi, S. Fally, J. Flaud, R. Gamache, A. Goldman, D. Jacquemart, I. Kleiner, N. Lacome, W. Lafferty, J. Mandin, S. Massie, S. Mikhailenko, C. Miller, N. Moazzen- Ahmadi, O. Naumenko, A. Nikitin, J. Orphal, V. Perevalov, A. Perrin, A. Predoi-Cross, C. Rinsland, M. Rotger, M. Simeckova, M. Smith, K. Sung, S. Tashkun, J. Tennyson, R. Toth, A. Vandaele, and J. Auwer, "The HITRAN 2008 molecular spectroscopic database," J. Quant. Spectrosc. Ra. Trans. **110**(9-10), 533–572 (2009).
25. X. Watremez, A. Marblé, T. Baron, X. Marcarian, D. Dubucq, L. Donnat, L. Cazes, P-Y. Foucher, R. Danno, D. Elie, M. Chamberland, J-P. Gagnon, L.B. Gay, J. Dobler, R. Ostrem, A. Russu, and M. Schmidt, "Remote Sensing Technologies for Detecting, Visualizing and Quantifying Gas Leaks," *In SPE International Conference and Exhibition on Health, Safety, Security, Environment, and Social Responsibility. Society of Petroleum Engineers* (2018).